Surface & Coatings Technology 460 (2023) 129432

Contents lists available at ScienceDirect

Surface & Coatings Technology

journal homepage: www.elsevier.com/locate/surfcoat

Investigation of the morphologies of chelate flame-sprayed metal oxide splats

YanXin Dan [a,b], XiaoMei Liu [a,b,*], Yu Wang [c], Jing Huang [a,b,*], Hidetoshi Saitoh [c], Yi Liu [a,b], Hua Li [a,b,*]

[a] *Key Laboratory of Marine Materials and Related Technologies, Ningbo Institute of Materials Technology and Engineering, Chinese Academy of Sciences, Ningbo 315201, China*

[b] *Zhejiang Engineering Research Center for Biomedical Materials, Cixi Institute of Biomedical Engineering, Ningbo Institute of Materials Technology and Engineering, Chinese Academy of Sciences, Cixi 315300, China*

[c] *Department of Materials Science and Technology, Graduate School of Engineering, Nagaoka University of Technology, 1603-1 Kamitomioka-machi, Nagaoka, Niigata 940-2188, Japan*

ARTICLE INFO

Keywords:
Splat morphology
Microstructure
Splashing
Droplet cooling
Flame spraying

ABSTRACT

This paper reports an investigation of Er_2O_3 splats formed by metal–ethylenediaminetetraacetic acid (EDTA) complex particles that were applied onto aluminum alloy substrates by flame spraying. The splat morphologies and coating microstructures were analyzed under different conditions. The effects of the in-flight particle temperature of the carrier gases and the impact particle deposition temperature on solidification of the molten droplets were evaluated with a rotating dodecahedron stage operated at velocities of 30, 75, and 90 rpm and with different temperatures and angles of incidence. Various techniques were used to analyze the surfaces and cross sections of the splats and coatings formed under the different conditions. Most of the splats underwent transitions from disk shapes (ratio > 85 %) to irregular shapes (circularity of 0.61–0.80) with increasing rotational velocity. The spray process provided a coating with a porosity of 23.3 % at a powder flow rate of 20 g/min. The temperature reached during the chelate flame spraying (CFS) process and the condensing velocity of the deposited splat, rather than the in-flight particle temperature, were found to control the splat morphology. This synergistic condensation effect paves the way to successful deposition of high-temperature structural ceramic coatings such as Er_2O_3 with the CFS method.

1. Introduction

Sprayed airborne particles undergo heating and acceleration after injection into the thermal plume during applications of thermal spray coatings [1]. The molten (or semimolten) droplets are propelled toward the substrate at high speeds. On impact, the droplets form splats, i.e., they rapidly spread and solidify on the substrate. During deposition, the buildup of these individual splats leads to the formation of coatings (or films) with the required surface characteristics. Therefore, splats with various morphologies and shapes provide the foundation of the coating [2–5]. The morphologies and shapes of the deposited splats depend on multiple factors: the high-temperature thermal-physical properties of the powder material (especially ceramics, with melting points > 2100 °C), the substrate temperature, and the droplet solidification characteristics [1]. A number of studies have been focused on contact by droplets sprayed perpendicular to the substrate surface and neglected the angle of incidence [6–9]. Most microstructural studies on the effects of these parameters on the splat morphology have involved particle deposition by plasma spraying due to its wide range of temperatures (typically from 8700 °C to 12,000 °C) [10,11]; thus, many powder materials are fully melted. Generally, the coatings formed by the plasma spray processes are dense and exhibit lower porosity (porosity <1 %) than those deposited by combustion processes [12–14]. However, these qualities make it difficult to synthesize any required coatings or microstructures, such as porous coatings (porosity>30 %), and the high energy consumption and cumbersome processes further limit the application of these methods [15,16]. Thus, the development of a new spraying method for depositing metal-oxide coatings that provides

* Corresponding authors at: Key Laboratory of Marine Materials and Related Technologies, Ningbo Institute of Materials Technology and Engineering, Chinese Academy of Sciences, Ningbo 315201, China.

E-mail addresses: liuxiaomei@nimte.ac.cn (X. Liu), huangj@nimte.ac.cn (J. Huang), Lihua@nimte.ac.cn (H. Li).

https://doi.org/10.1016/j.surfcoat.2023.129432
Received 2 November 2022; Received in revised form 13 March 2023; Accepted 14 March 2023
Available online 20 March 2023
0257-8972/

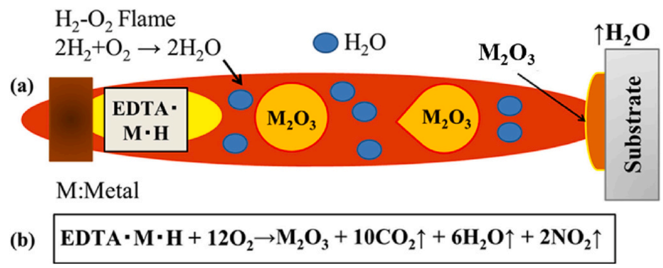

Fig. 1. (a) Model image for the synthesis of M_2O_3 by the chelate flame spraying process. (b) The chemical reaction of EDTA·M·H.

stability, such as thermal corrosion resistance, is still a great challenge.

A mixture of H_2–O_2 or C_2H_2–O_2 is commonly used as the combustion gas in flame spraying, which restricts the flame stream to relatively moderate temperatures (typically approximately 2300 °C) [17]. The restricted temperatures make this deposition method inapplicable to ceramic coatings prepared by high-temperature melting, such as yttrium oxide [18,19]. Therefore, researchers have proposed a new spray process using a metal–ethylenediaminetetraacetic acid (EDTA) complex [1,20,21]. In this process, the metal–EDTA powders are introduced to the substrate by a flame-spraying method, so we refer to it as chelate flame spraying (CFS) [22]. During the CFS process, the complexed powders are placed into a feed unit (5 g/min-15 g/min) and transported by a flowing carrier gas (air, N_2 or O_2) into the flame plume [23]. These metal–EDTA powders decompose and oxidize in the flame and form metal oxide particles, which are subsequently deposited on the substrate. However, the lower surface temperature of the substrate in the chelate flame spraying process results from the H_2O (water) generated in (a) the reaction of H_2 and O_2 in the H_2–O_2 flame and (b) the decomposition reactions of the raw materials (EDTA·M·H, M: metal), as shown in Fig. 1. Moreover, acetylene burns too early and is not hot enough, the precursors cannot completely decompose the raw materials (EDTA), and the H_2-O_2 flame is more conducive to the preparation of clean coatings with no carbon residues. Therefore, it is of great significance to systematically study the morphology of a coating on a low melting substrate, such as an aluminum alloy, by the CFS method. The splat deposition process fundamentally consists of particles and droplets impacting the substrate and then spreading and solidifying [24]. The present study investigates the influence of the preparation parameters on the coating, such as a powder flow rate of 5 g/min and an O_2 carrier gas with a flow rate of 7.1 L/min, which are used to deposit dense coatings with low porosity <3 % [1]. The above results mean that the splat particles can be changed to design the structure of the oxide ceramic coating (Y_2O_3 and Er_2O_3) by controlling the decomposition mechanism of EDTA; apparently, EDTA works better, and the flame spraying method overcomes the difficulty of preparing coatings with high melting points because the combustion and decomposition processes of the EDTA complex are exothermic [23]. In previous studies, we used the CFS method to synthesize ceramic materials (Y_2O_3 and Er_2O_3) and deposited coatings with cross-sectional porosities of 2–33 % on different substrates, such as stainless steel, aluminum alloys and quartz [24–26]. Furthermore, droplet spreading played a key role in determining the microstructure, including the shapes and sizes of the pores and gaps between the splats of the deposited coatings. In previous studies, the cost of a CFS-sprayed Y_2O_3 coating was similar to or greater than that of a thermal barrier coating synthesized with an atmospheric plasma spray (APS) method [25,27,28]. Additionally, deposited Y_2O_3 coatings exhibited strong adhesion and good thermal shock resistance on aluminum alloy substrates [29,30]. Moreover, there was evidence that the splat morphologies were correlated with coating density, coating deposition efficiency and pores and oxide inclusions. Choosing the ideal carrier gas (N_2) and spray distance was shown to be an efficient and cost-effective way to alter the properties of the splats from fragmented to more desirable disk morphologies [22]. Other behaviors in CFS, such as the particle impact styles, are still not fully understood. Thus, there is still a need to establish quantitative correlations between splat morphologies and shapes and coating microstructures to achieve optimal designs.

Few studies have described the development of splat morphology and microstructure by using CFS with the process parameters used in this study. Herein, Er_2O_3 splats and coatings were deposited by CFS onto aluminum alloy substrates. The impact angles of the airborne particles and droplets were set with a rotation apparatus (dodecahedral pattern) with rotational velocities of 30, 75 and 90 rpm. The overarching aim of this study was to investigate the spreading behavior of EDTA·Er·H raw materials with different cooling modes (fixation and rotation) and spraying parameters. To assess the circularity, the proportion of disk-like splats, the splat particle sizes and the microstructures of the Er_2O_3 splats and thick coatings, and the cross-sectional splat-substrate features were analyzed with scanning electron microscopy (SEM) and a watershed algorithm. We explained the effects of the CFS process parameters, including impact types and airborne particle temperatures, on the characteristics of the ceramic coating.

2. Experimental procedure

The powder feedstocks for the metal–EDTA complex, EDTA·Er·H (Chubu Chelest *Co.*, Ltd.), were flame sprayed onto a polished aluminum alloy (A5052, 50 × 50 × 5 mm^3) substrate. The chelate materials were synthesized with the following method. First, a stoichiometric amount of ethylenediaminetetraacetic acid disodium salt (EDTA-2Na, 99 %) was dissolved in 60 mL of D.I. water under constant magnetic stirring at room temperature. The concentration of the original solution was 0.1 M. To this solution, 1 M NaOH solution was added dropwise to maintain a pH of 11.5–13, which was monitored with a pH meter (METTLER-TOLEDO–PE20K), and this solution was labelled A. Afterward, an equivalent molar ratio of erbium nitrate hexahydrate ($Er(NO_3)_3.6H_2O$, 99 %) was dissolved in 50 mL of D.I. water under constant magnetic stirring, a transparent solution formed and the solution was allowed to stir for an additional half an hour. Then, the transparent solution was mixed with solution (A) and placed at room temperature for 8–14 h. A

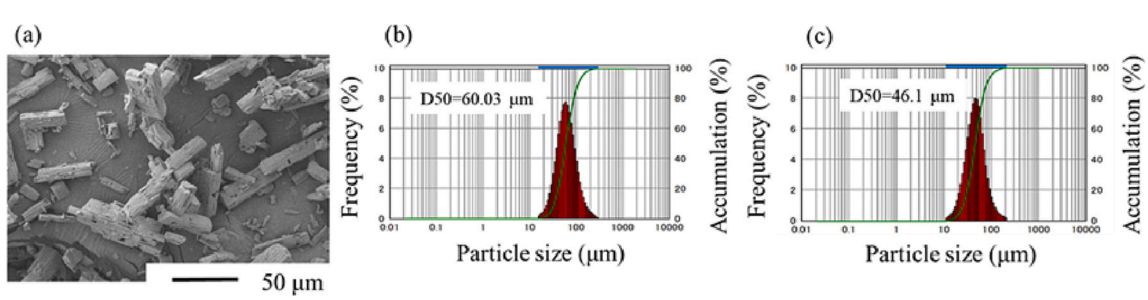

Fig. 2. (a) Powder state of the raw material EDTA·Er·H, (b) particle size distribution of the unscreened powder, and (c) particle size distribution of the 45 μm material.

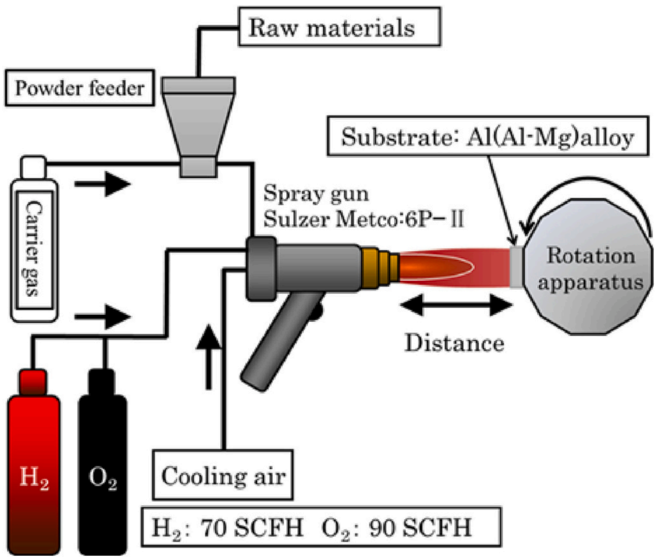

Fig. 3. Schematic of the coating deposition apparatus with a rotating stage.

white precipitate was formed. The solid white precipitate was collected and washed with D.I. water and ethanol several times and oven-dried at 90 °C for 5–8 h. The obtained sample was ground to form a fine powder.

The substrate surface was cleaned twice with acetone. The experimental setup used to deposit these splats can be described in a previous study [22]. We used 45-μm raw materials and unscreened EDTA·Er·H powder to perform the splat tests, as shown in Fig. 2 (a). In addition, to study the relationship between substrate temperature and particle morphology, we used the aforementioned flame spray equipment and a 12-sided rotating stage on which the substrate was fixed; the substrate temperature was reduced by rotation, as shown in Fig. 3.

Tables 1 and 2 list the parameters (powder flow rate, rotational velocity and velocity of the substrate) for the carrier gases (O_2 and N_2) that were used to deposit the 45-μm raw materials and unscreened EDTA·Er·H powder on the individual Er_2O_3 splats; the particle sizes are shown in Fig. 2 (b) and (c). To study the relationships between the individual splat morphologies and the coating structures, Er_2O_3 coatings were deposited via a CFS system with a rolling velocity of 90 rpm; the spraying parameters are listed in Table 3.

The phases of the various synthesized coatings were characterized by X-ray diffraction (XRD, M03XHF22, Japan) with Cu-Kα radiation over a 2θ range of 10–90°. A range of microscopic techniques, including field-emission scanning electron microscopy (FE-SEM), was employed to observe the surface morphologies and cross sections of the splats and coatings. To study the morphologies of the splats, the SEM images were binarized with ImageJ to display the A5052 substrate and the splats with different colors, such as white and black. Furthermore, the overlapped splats in the binarized surface images were separated with the watershed algorithm. Afterward, the various morphological parameters of the splats were calculated from the surface images [31]; this technique was applied in our previous studies [22]. Important information about the splats was estimated from many surface images to obtain accurate values. The circularity was calculated with Eq. (1):

$$\text{Circularity} = \frac{4\pi A}{p^2} \tag{1}$$

where A is the area of the splat and P is the perimeter of the splat. Then, a boundary tracking algorithm was used to determine the boundaries from the image contours obtained by binarizing the P regions with ImageJ software. In addition, when the shape of a splat was similar to that of a disk, the primary slat circularity approached one, and distorted splats had low circularities [22]. SmileView and ImageJ software were used for quantitative analyses of the Er_2O_3 coating microstructures.

3. Results and discussion

The use of O_2 as the carrier gas not only increased the flame temperature but also facilitated rapid decomposition and oxidation of the chelate powder. The temperature of the in-flight particles was approximately 2400 °C, which was higher than that produced by using N_2 as the carrier gas [23]. The raw materials of metal-EDTA complexes were placed in a feed unit and transported by the flowing carrier gas (N_2 or O_2) to the spray gun. The gas–solid mixture was introduced into a H_2-O_2 flame and reacted with oxygen after thermal decomposition of the EDTA in the CFS process. Moreover, in the chemical reaction of the metal–EDTA complex powder in the flame, the EDTA·Er·H mixture reacted with O_2 to form a metal oxide film, as shown in Eq. (2):

$$2\text{EDTA}\cdot\text{Er}\cdot\text{H} + 24\text{O}_2 \rightarrow \text{Er}_2\text{O}_3 + 20\text{CO}_2 + 13\text{H}_2\text{O} + 4\text{NO}_2 \tag{2}$$

Therefore, when the carrier gas was changed from O_2 to N_2, the reaction was inhibited, the thermal energy of the in-flight particles decreased, and the particle temperature decreased. These changes in the temperature of the impacting particles are expected to exert the greatest effect on droplet spreading. Additionally, the jet entrained large amounts of air, and the reaction still occurred in the N_2 carrier gas.

3.1. Changes in the splats with different powder flow rates

Fig. 4 (a–d) shows the typical morphologies of the Er_2O_3 splats produced at powder feed rates of 5, 10, 15 and 20 g/min when the carrier gas was O_2. There were no significant macroscopic differences in the splat morphologies due to the different powder feed rates. When N_2 was used as the carrier gas, the numbers and sizes of the splats decreased as the feed rate of the powder was increased, as shown in Fig. 4 (h–k). In contrast, when different gases were combined with the O_2 and N_2, there were significant differences in the morphologies of the particles and the number of splats. Table 4 shows the temperatures seen for the airborne particles at powder feed rates of 10 and 20 g/min with O_2 as the carrier gas. As the powder feed rate was increased from 10 to 20 g/min, the airborne particle temperature and velocity decreased. This was explained with Eq. (3), which was provided by F. Fanicchia et al. [32]; as the powder feed rate increased with M_{powder}, the loading effect increased. The increased loading effect was why the airborne particle velocity and temperature were determined with this method. Furthermore, the effect of the parameters for the airborne particles on particle melting is shown in Eqs. (3)–(6) [32,33]:

$$\int_0^\tau Q_{int} \cdot dt > Q_M \tag{3}$$

Table 1
Experimental conditions used to prepare splats via the deposition of EDTA·Er·H with different powder flow rates. O_2 was used as the carrier gas for samples (a)–(d), and N_2 was used as the carrier gas for samples (h)–(k).

No.	Method	Raw material	Flow rate of powder (g/min)	Flow rate of carrier gas (L/min)	Distance (mm)	Number of scans	Carrier gas
a/h	Fixed	Unscreened	5.0	7.1	150	1	O_2/N_2
b/i			10.0				
c/j			15.0				
d/k			20.0				

Table 2
Experimental conditions used to prepare splats via the deposition of EDTA·Er·H at different rotational velocities. O_2 was used as the carrier gas for samples (e)–(g), and N_2 was used as the carrier gas for samples (l)–(n).

No.	Method	Raw material	Flow rate of powder (g/min)	Flow rate of carrier gas (L/min)	Distance (mm)	Number of scans	Carrier gas	Rolling velocity (rpm)	Velocity of the substrate (m/s)
e/l								30	0.5
f/m	Roll	45 µm on	0.2	7.1	150	10	O_2 / N_2	75	1.25
g/n								90	1.5

Table 3
Parameters for the Er_2O_3 coating depositions.

Sample	Flow rate of powder (g/min)	Carrier gas type	Rolling velocity (rpm)	Distance (mm)	Flow rate of carrier gas (L/min)
(a)	20	O_2	90	150	7.1
(b)	20	N_2			

$$\tau = \frac{SOD}{V_p} \tag{4}$$

$$Q_{int} = h\left(\pi d_p{}^2\right)\left(T_\infty - T_p\right) - \left(\pi d_p{}^2\right)\epsilon\sigma_s\left(T_p{}^4 - T_\alpha{}^4\right)\ [W] \tag{5}$$

$$Q_M = \frac{4}{3}\pi\rho_p d_p{}^3\left(C_p(T_m - T_0) + L_m\right)\ [J] \tag{6}$$

where Q_{int} is the heat transferred to the particles during flight; Q_M is the heat required to melt the particles; τ is the in-flight dwell time of the particles; SOD is the stand-off distance; V_p is the particle velocity; d_p, ρ_p, and C_p are the particle diameter, density and specific heat, respectively; h is the convective heat transfer coefficient; T_∞ is the flame temperature at the particle surface; ε is the particle emissivity; σ_s is the Stefan–Boltzmann constant; T_p and T_α are the temperatures of the particle and surroundings, respectively; and T_m, T_0 and L_m are the particle melting temperature, initial temperature and latent heat of fusion, respectively. In Eqs. (3)–(6), intraparticle thermal conduction and oxidative behavior were neglected. Thus, when Q_{int} was higher than Q_M, the particles in the flame melted. These equations suggested that as the powder feed rate was increased, the loading effect would increase, and the temperature and velocity of the airborne particles would decrease. Moreover, a lower velocity led to a longer heating time and higher particle temperatures (unless the standoff distance was too large so that excessive cooling occurred) in the traditional spray flame. However, these effects decreased the amount of heat transferred (Qint) (due to cooling of the flame by the higher feed rate) in spite of the lower particle velocity and longer residence time in the flame, which negatively affected splat melting and diffusion in the chelate spraying process, perhaps by affecting the EDTA decomposition rate. Thus, as the powder feed rate was increased, the temperature of the airborne particles was expected to decrease, and diffusion during the splat formation deteriorated. However, based on rapid splat solidification according to the thermal conductivity of the A5052 substrate, we expected that the proportions of splash-like particles, unmelted particles and resolidified splats would increase because the feed rate increased, which indicated that during the impact and deposition of particles, those particles that did not flatten were detached from the substrate.

Furthermore, the circularities and proportions of the disk-like splats and the splat sizes were measured from SEM images of the surface (Fig. 4), as listed in Table 5. The use of N_2 as the carrier gas increased the circularities and proportions of the disk-like splats with increasing powder feed rate. Moreover, splashing was likely if the solidification was not fast, which happens with warmer substrates or superheated melts, such as when O_2 is used as the carrier gas (shown in Fig. 4(a)). According to this analysis, the M_{powder} and Q_{int} values of the airborne particles increased, which resulted in a lower temperature for each particle. Additionally, the measurement results showed that when the powder flow rate was 15 g/min, the splats all exhibited higher disk-like ratios when N_2 and O_2 were used as the carrier gases. Thus, the temperatures were not sufficiently high for all of the airborne particles to reach the melting point and decompose the EDTA·Er·H. This was consistent with the results of our previous studies [1]. This meant that a powder feed rate of 15 g/min was the cutoff point in this study. Additionally, the adhesion rate decreased at a powder feed rate of 20 g/min. Therefore, it is reasonable to hypothesize that the powder feed rate of the EDTA·Er·H and carrier gas used in this study controlled the

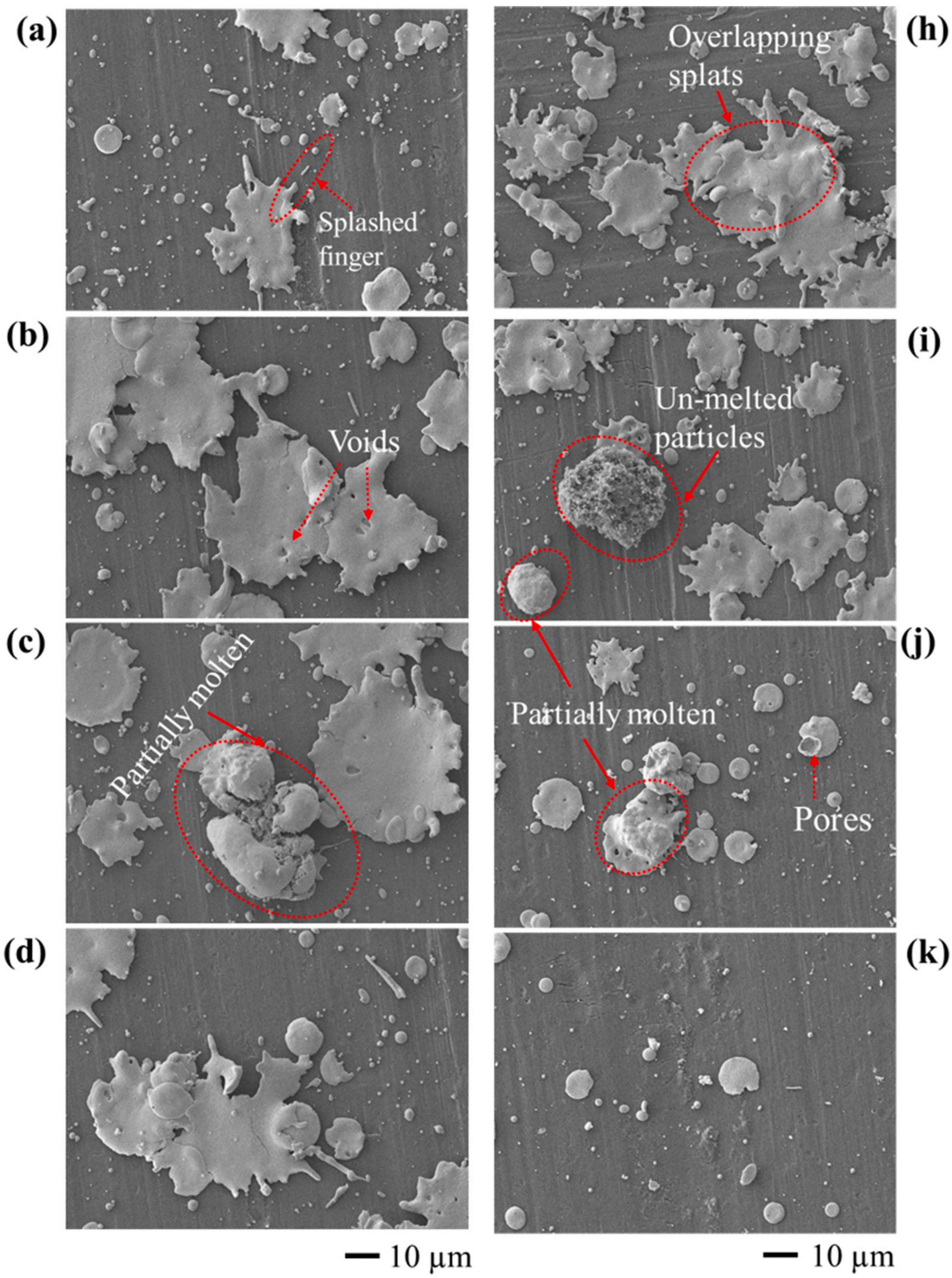

Fig. 4. Images of the surfaces of Er_2O_3 splats deposited on the A5052 substrate at different powder flow rates.; O_2 (a)/N_2 (h): 5 g/min, O_2 (b)/N_2 (i): 10 g/min, O_2 (c)/N_2 (j): 15 g/min, and O_2 (d)/N_2 (k): 20 g/min.

Table 4
Temperature changes of the in-flight particles in the EDTA·Er·H powder with different spray distances and powder feed rates while using O_2 as the carrier gas.

Nozzle-substrate Distance (mm)	In-flight particle	10 g/min	20 g/min
110	Temperature (°C)	2600	2200
	Velocity (m/s)	230	92
130	Temperature (°C)	2640	2300
	Velocity (m/s)	170	90
150	Temperature (°C)	2610	2400
	Velocity (m/s)	115	86
170	Temperature (°C)	2550	2420
	Velocity (m/s)	85	80

Table 5
Results for the samples in which Er_2O_3 splats were deposited on the A5052 substrate with different powder flow rates.

No./ Carrier gas	Flow rate of powder (g/min)	Circularity /SD (−)	Disk-like ratio /SD (%)	Splat particle size /SD (μm)
(a)/O_2	5.0	0.66/0.02	65.8/4.6	15.4/1.1
(b)/O_2	10.0	0.67/0.01	66.8/3.6	16.4/0.4
(c)/O_2	15.0	0.70/0.01	71.6/2.1	17.3/0.9
(d)/O_2	20.0	0.67/0.01	65.8/3.0	16.8/0.8
(h)/N_2	5.0	0.66/0.01	63.6/2.5	15.4/0.4
(i)/N_2	10.0	0.70/0.02	75.0/2.5	13.6/0.6
(j)/N_2	15.0	0.79/0.01	88.5/1.1	11.6/0.4
(k)/N_2	20.0	0.80/0.04	87.9/4.8	10.2/0.2

deposition of porous or dense splats.

3.2. Changes in the splat state as a function of the rotational velocity

Fig. 5 shows SEM images of the surfaces of the coatings sprayed on the A5052 substrate with O_2 carrier gas (samples (e), (f), and (g)) and N_2 carrier gas (samples (l), (m), and (n)). In a previous study, we used a contact thermometer to measure the temperature of the substrate after spraying at 579, 454, and 441 K for each rotational speed (30, 75, and 90 rpm, respectively) [25].

In the SEM images showing the surface morphologies of the Er_2O_3 splats, the types of deposited splats differed significantly (finger-shaped, splash-shaped, voided, microcracked, partially molten, and malformed splats). When O_2 was the carrier gas, a shattered splatter deposition and splashing pattern upon impact was observed when the rotational velocity was 30 rpm, as shown in Fig. 5 (e). In addition, the splats were transformed from shattered splatters to disk-shaped splatters as the rotational velocity was increased from 75 to 90 rpm (shown in Table 2) due to the velocity of the substrate; this was much lower than the particle velocity, resulting in a faster cooling rate, as shown in Fig. 5 (f), (g). However, when N_2 was the carrier gas, the microstructures in the deposited disk-shaped splats were relatively uniform. In contrast to the use of O_2 as the carrier gas, the splat diameters of the deposits decreased as the rotation speed increased. Overlaps and microcracking were clearly observed in Fig. 5 (l). Moreover, ideal disk-shaped splats were observed on the A5052 substrate when a rotational velocity of 30 rpm was used, which was similar to the observations reported by Markus Mutter et al. [34] for the use of the plasma spraying method. With a rotational velocity of 75 rpm, there was some molten material in the splats, as shown in Fig. 5 (f). The long fingers in the splat were clearly formed at high rotational velocities (90 rpm) and were observed in the SEM photographs shown in Fig. 5 (n). This could have been caused by molten particles impacting the substrate as it rotated at high speed and applied a rotational force on the deposited splats [35]. Notably, the majority of the splats on the substrates were formed from fully melted particles, and some splats were disk-shaped, which was similar to the morphologies of plasma-sprayed splats [36]. However, the splats resulting from freezing-induced splashing had different appearances than those that fragmented during impact (Fig. 5 (g) and (n)). Thus, when the molten particles impacted the lower temperature substrate, instant coagulation occurred, and the number of irregular boundaries increased. For the above case, the deposited splat size was greater when the N_2 carrier gas was used than when the O_2 carrier gas was used. Additionally, it can be inferred from Fig. 5 (n) that the splat with larger fingers radiating out from its periphery was formed with a higher rotational velocity; additionally, spreading was considerably faster than solidification.

In addition, the surface images were used to calculate the degrees of circularity, the proportions of disk-like splats, and the splat sizes of the particles deposited at different rotational velocities with O_2 and N_2 carrier gases (Eq. 1); the results are shown in Table 6. According to the results of the calculations, the circularities of the slats and the proportions of disk-like slats decreased below 75 rpm for both the O_2 and N_2 carrier gases. In the case of 90 rpm rotation, these values increased. In comparison, the splat morphologies showed greater degrees of circularity and smaller disk-like splat particles when O_2 rather than N_2 was used the carrier gas. In addition, for both gases, as the number of rotations increased, the splat sizes decreased, and the largest splat diameters were 10–15 μm, as shown in Fig. 6. The chart in Fig. 7 shows the circularities of the Er_2O_3 splats deposited on the A5052 substrates at different rotational velocities. When O_2 was used as the carrier gas, the splats with circularities of 0.8 (from 0.7 to 0.79) were increased in abundance as the rotational velocity increased. The number of splats with circularities of 0.9 (from 0.8 to 0.89) was clearly increased at rotational velocities of 30 and 90 rpm. Furthermore, splats with circularities of 0.6 (from 0.5 to 0.59), 0.7 (from 0.6 to 0.69), and 0.9 (from 0.8 to 0.89) increased in number as the rotational velocity increased with N_2 used as the carrier gas. Finally, when O_2 was the carrier gas, there were more splats with a greater circularity and a greater proportion of small splats compared to when N_2 was the carrier gas. Furthermore, the distribution of the splat particle sizes was narrower when O_2 was the carrier gas.

The effects of the rotational velocity (rpm) on the circularities and proportions of disk-like splats and the splat particle sizes are shown in Fig. 8. The circularities and proportions of disk-like splats were lower with a rotational velocity of 75 rpm; in contrast, these parameters were increased at 90 rpm for the O_2 and N_2 carrier gases. In addition, the splat particle sizes decreased with the rotational velocity, as shown in Fig. 8 (c). This occurred because the rotational velocity increased as the substrate temperature decreased, and the results are shown in Table 7. When the rotational velocity was increased to reduce the scan time corresponding to the flame, the substrate temperature during deposition decreased. When the substrate temperature decreased, the temperature gradient between the splat and the substrate increased, and the effect of the cooling rate increased. Therefore, when the airborne particles impacted the substrate, they solidified or became partially solidified before they flattened, so the number of splashes or splats that were not flattened decreased. With the above conditions, the proportion of splats with splash-like shapes increased, and the circularity and the proportion of the disk-like splats decreased at a rotational velocity of 75 rpm. In addition, since the splat particle sizes decreased, the number of resolidified particles increased. At 90 rpm, the splat particle sizes continued to decrease, the numbers of resolidified particles and nonflat splats increased, and the circularities increased on the surface; thus, the circularity and proportion of disk-like splats also increased. Depending on the rotational velocity, this behavior might cause an increase in the coating porosity.

3.3. Microstructure of the coating

During deposition, the in-flight particles that fully absorbed heat while passing through the flame zone melted fully and were spread uniformly and completely upon impacting the substrate surface, which produced a smooth, flat, dense fully melted zone [37]. Thus, the majority of ceramic coatings with high melting points can be prepared by

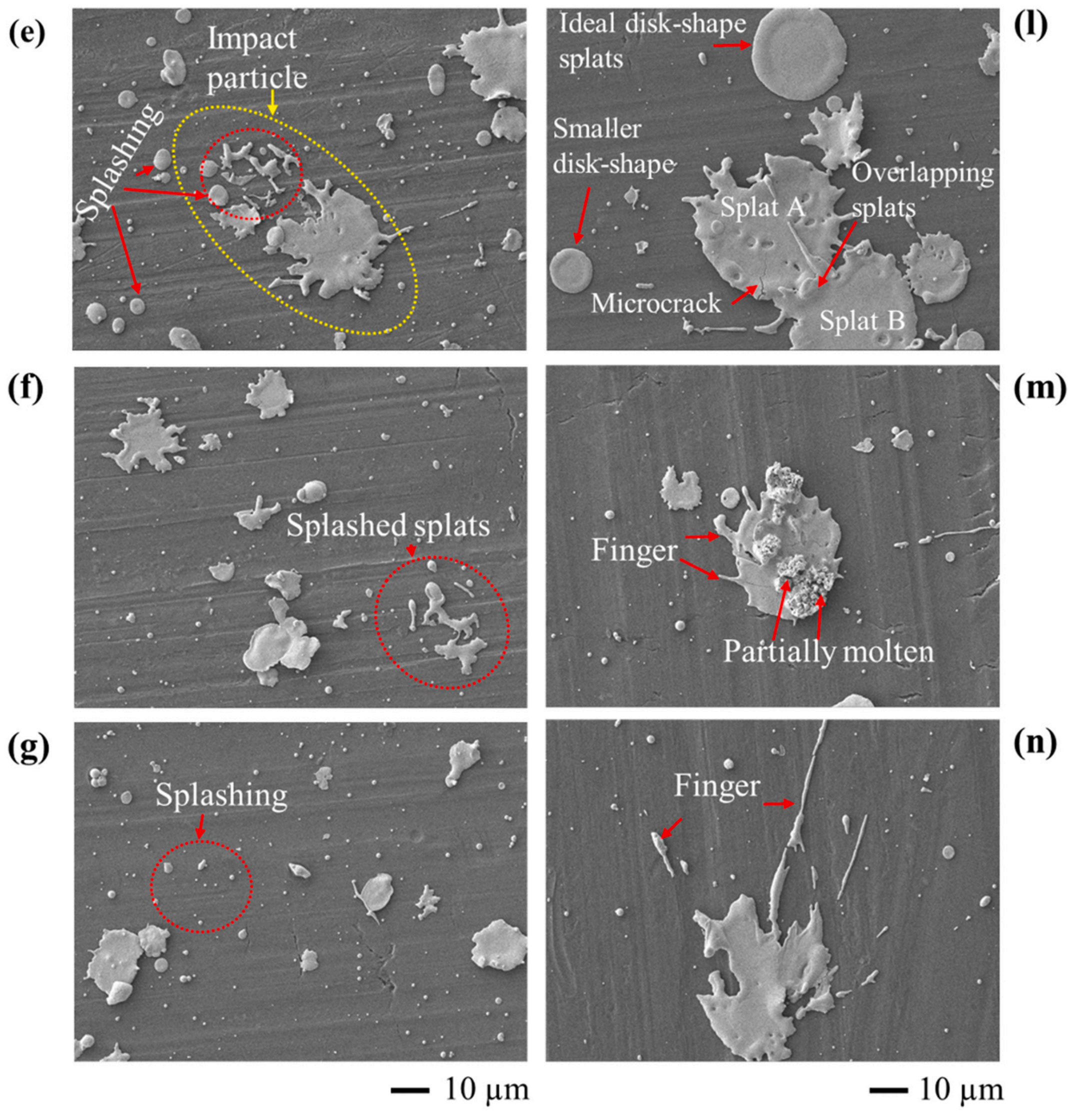

Fig. 5. SEM images of the surfaces of Er_2O_3 splats deposited on the A5052 substrate at different rotational velocities; O_2 (e)/N_2 (l): 30 rpm, O_2 (f)/N_2 (m): 75 rpm, and O_2 (g)/N_2 (n): 90 rpm.

Table 6
Results for samples in which the Er_2O_3 splats were deposited on the A5052 substrate at different rotational velocities.

No./ Carrier gas	Rolling velocity (rpm)	Circularity /SD (–)	Disk-like ratio /SD (%)	Splat particle size /SD (μm)
(e)/O_2	30	0.72/0.01	77.7/4.0	12.0/0.5
(f)/O_2	75	0.70/0.00	74.3/3.5	10.4/0.4
(g)/O_2	90	0.74/0.02	84.1/7.2	10.2/0.5
(l)/N_2	30	0.70/0.02	69.7/6.4	17.3/0.7
(m)/N_2	75	0.66/0.00	61.8/5.3	14.4/0.4
(n)/N_2	90	0.70/0.01	73.1/1.11	13.8/1.8

plasma spraying [36,38]. The combination of physical and chemical means, such as the pyrolysis of precursors in the early stage and oxidation in the middle stage, as well as regulation of the parameters related to the impact of flying particles on the substrate in the later stage. It will be more promising to realize the preparation and design of ceramic coatings such as those prepared by the EDTA method if the method is applied to lower melting temperature materials. The XRD patterns of the Er_2O_3 coatings are shown in Fig. 9. The peaks in the XRD profiles were assigned by using International Centre for Diffraction Data (ICDD) cards as references. The deposited Er_2O_3 coating exhibited a cubic crystalline phase (ICDD, No. 00–008-0050). The XRD spectra always contained peaks corresponding to the original phase of the coating used with N_2 or O_2 as the carrier gas at a rotation speed of 90 rpm, indicating that the coating did not differ from that obtained without the rotating stage [1]. In addition, the peak intensity of the coating phase hardly changed with changes in the spraying conditions.

To verify the influence of the splat morphologies described above on the coating microstructures, coatings were produced with the two carrier gases at a rotational velocity of 90 rpm and a powder flow rate of 20 g/min. Fig. 10 shows that the microstructures of the coatings were significantly different in these cases. Compared to the results obtained with O_2 as the carrier gas, more large pores and meshwork were observed in the coating made with N_2 as the carrier gas, as shown in Fig. 10 (a) and (b). A rotation splat interfacial line was formed, and the line was marked, as shown at high magnification in Fig. 10 (a_1). Moreover, the same microstructure can be observed in Fig. 10(a_2). The irregular shapes of splats clearly overlapped to form large voids between the splats, as shown in Fig. 10 (b_1) and (b_2), which was consistent with the morphologies of the individual splats (Fig. 5(n)). Additionally, with the decreases in substrate and in-flight particle temperatures, the proportion of meshwork structures increased, as shown in Fig. 10, which

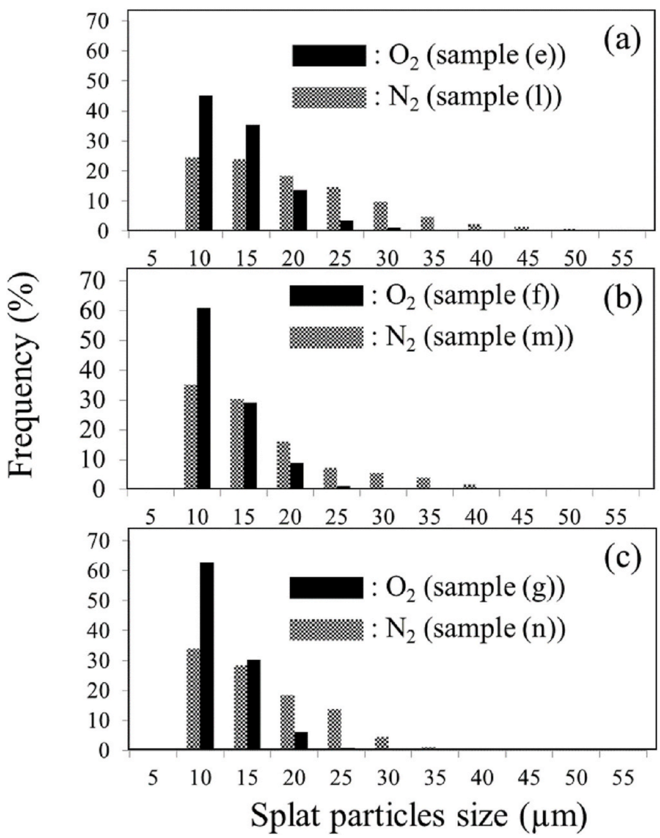

Fig. 6. Particle sizes of the Er_2O_3 splats deposited on the A5052 substrate at different rotational velocities: (a) 30 rpm, (b) 75 rpm, and (c) 90 rpm.

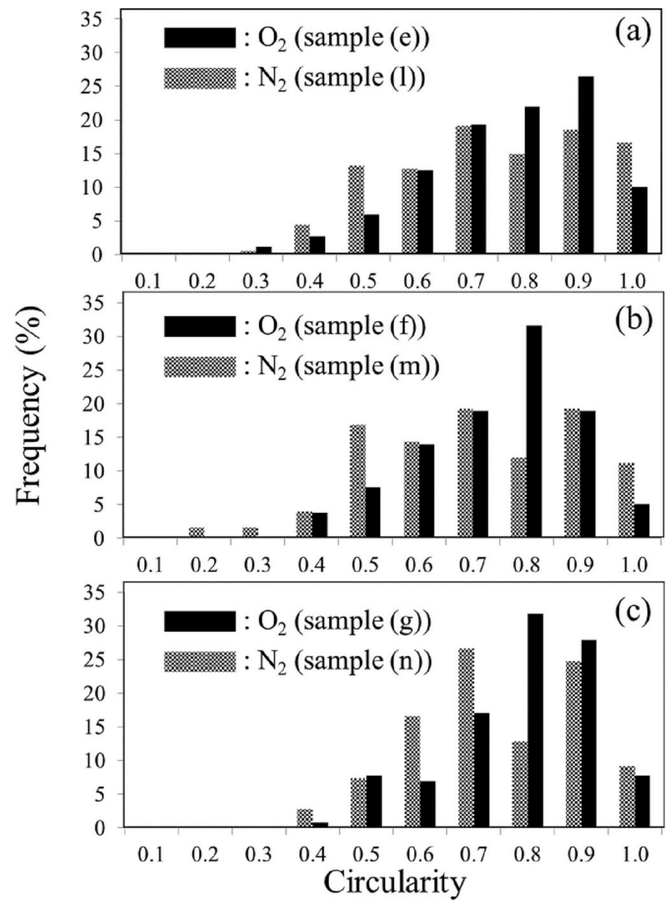

Fig. 7. Circularities of the Er_2O_3 splats deposited on the A5052 substrate at different rolling velocities: (a) 30 rpm, (b) 75 rpm, and (c) 90 rpm.

was roughly consistent with a previous study of the meshwork resulting from a coating deposition process [1]. Moreover, with the cross-sectional images, we evaluated the thicknesses and porosities of the coatings. The sample in Fig. 10 (b) had a porosity more than two times greater than the porosity of the sample in Fig. 10 (a), which exhibited a porosity of 23.3 %. The details are listed in Table 8. Based on these results, it was evident that the microstructures of the coatings differed because of the lower in-flight particle temperatures. After impact, the droplets began to spread as a result of inertia due to the substrate rotation. In other words, after impinging the rotating substrate, the droplets quickly began to flatten and formed irregular shapes during solidification. This was accompanied by simultaneous losses of kinetic and thermal energies, which led to the differences observed for the solidified morphologies of the splats and built-up porous coatings. As mentioned above, airborne metal–EDTA particles that fully absorb heat decompose, oxidize, and melt thoroughly in CFS systems. Thus, the droplet impact styles play a significant role in defining the spreading behavior at the periphery of a splat. Therefore, it is reasonable to assume that the CFS method has promise for synthesizing high-quality structural ceramic coatings.

4. Conclusions

In this study, Er_2O_3 splats and thick coatings were prepared with CFS. The spreading behavior of a metal–EDTA complex mixed powder sprayed on an A5052 substrate was investigated. The following is a summary of the findings:

- The majority of the Er_2O_3 splats were formed from fully melted particles and exhibited typical morphologies in both carrier gases, such as disk- and splash-shaped morphologies. Since relatively less splashing was observed when N_2 was used as the carrier gas, the droplets prepared with O_2 spread more easily and formed fragmented splats due to overmelting. However, the effect became less pronounced as the flow rate of the powder was increased from 5 to 20 g/min. The rotations decreased the substrate temperature and modified the splats formed by enhancing droplet melting during spreading.
- When O_2 was used as the carrier gas with high-speed rotation (90 rpm), the Er_2O_3 coating had a whirl-like lamellar structure and some porosity (10.3 %). When N_2 was used as the carrier gas, the coating porosity increased (23.3 %) with increasing irregularity of the splat morphology because of the mode of solidification. Therefore, the morphologies and characteristics of the splats (such as the circularities and proportions of the disk-like splats) had direct effects on the coating microstructures deposited by CFS.

In summary, flower-like splats and disk-like splats were often formed by droplets with appropriate cooling velocities after impacting the substrate. Moreover, compared with traditional melted raw materials and parameter control methods, the CFS system leads to more complex coating deposition behavior, so more key factors, such as the decomposition speed of the metal–EDTA complex, must be explored to evaluate this flame spraying method completely.

CRediT authorship contribution statement

Yanxin Dan: Conducting a research and investigation process; Preparation.

Xiaomei Liu: specifically critical review.

Yu Wang: Management activities to annotate (produce metadata);

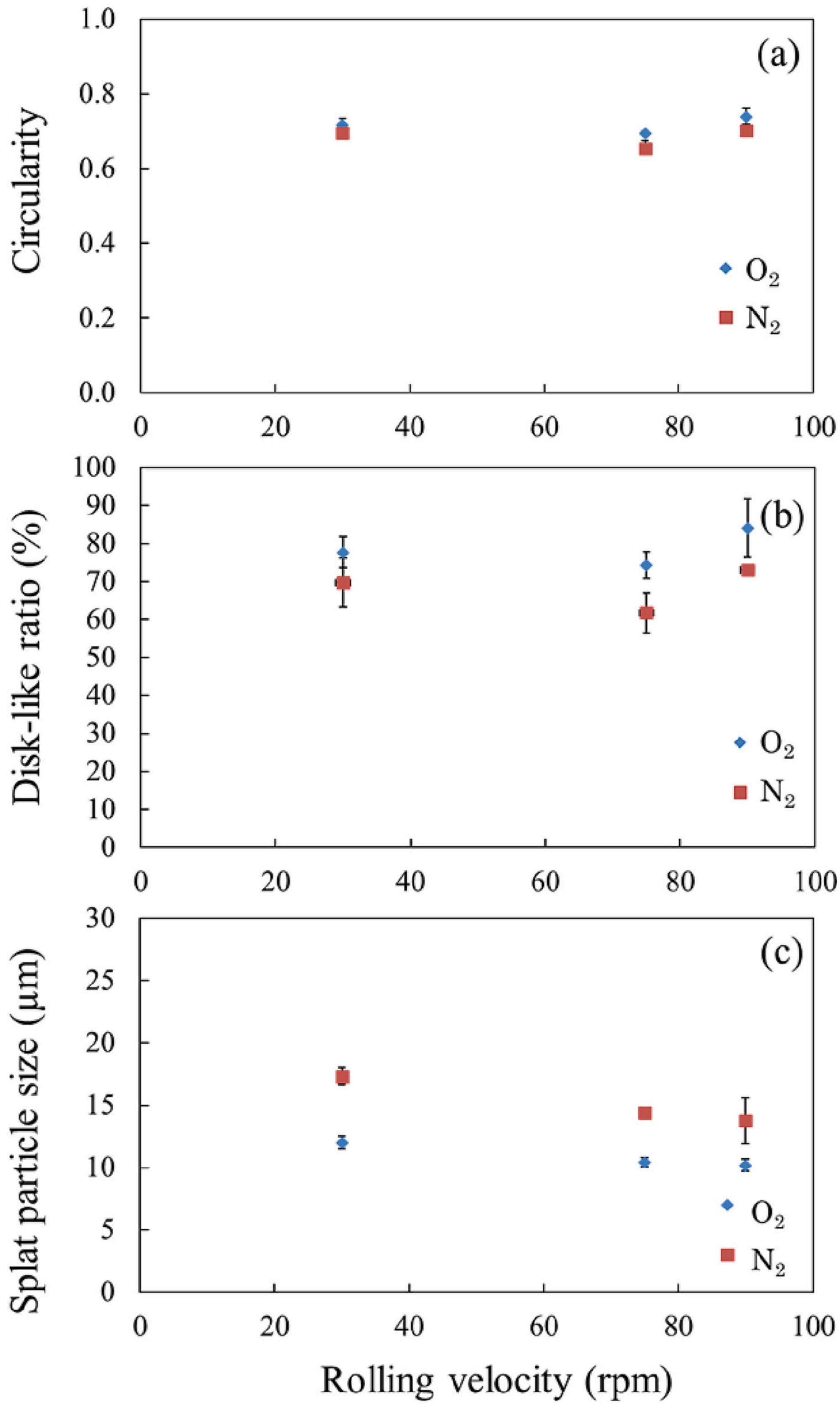

Fig. 8. Results for Er_2O_3 splats deposited on the A5052 substrate at different rotational velocities; (a) Splat circularity, (b) proportion of disk-like splats, and (c) splat particle size.

Table 7
Substrate temperatures for various rolling velocities.

Rolling velocity (rpm)	Substrate temperature /SD (°C)
30	306/3.1
75	181/2.9
90	168/1.2

Application of statistical.

Jing Huang: Provision of study materials.

Hidetoshi Saitoh: Ideas.

Yi Liu: Acquisition of the financial support for the project leading to this publication.

Hua Li: Formulation or evolution of overarching research goals and aims.

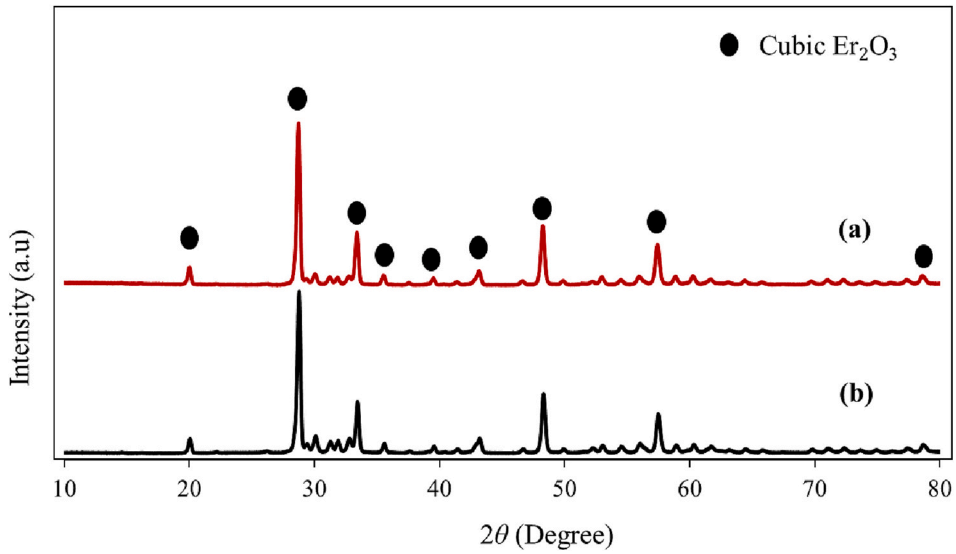

Fig. 9. XRD patterns of Er_2O_3 prepared by CFS at 90 rpm with different carrier gases; (a) O_2 as the carrier gas, and (b) N_2 as the carrier gas.

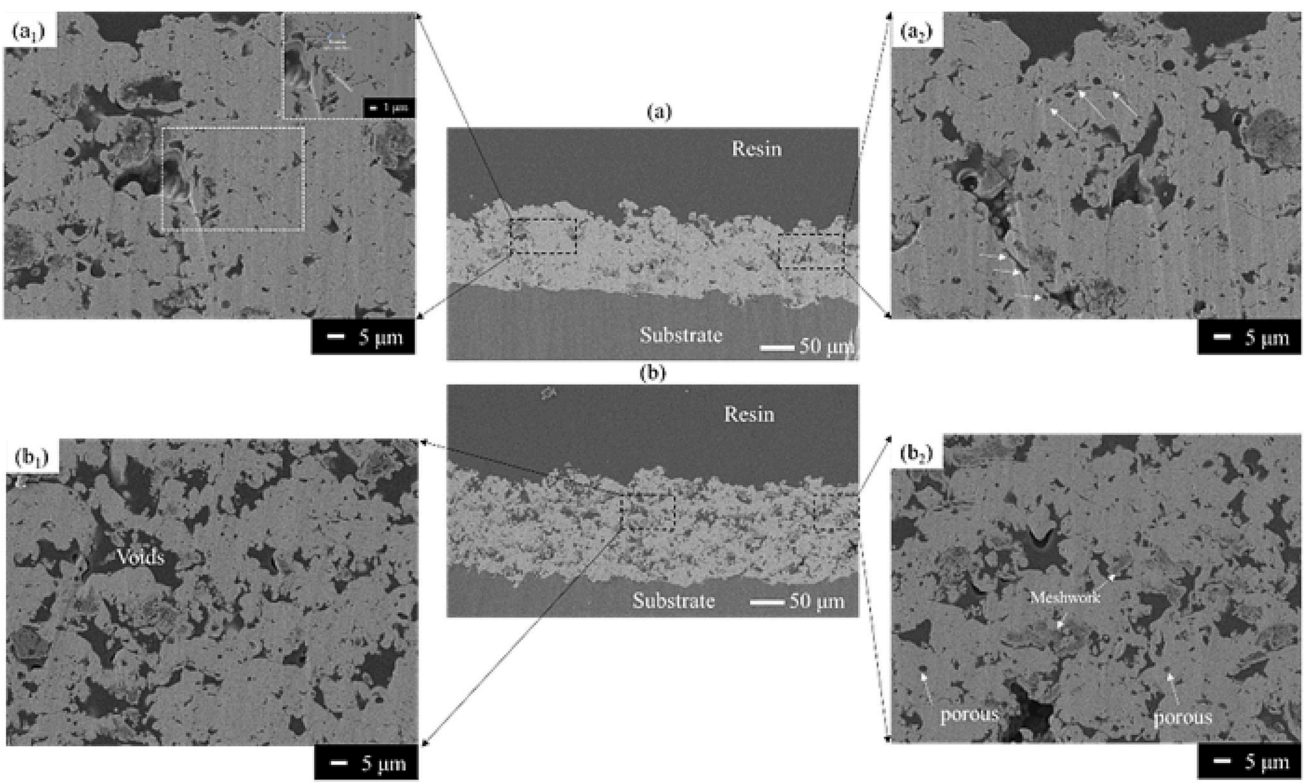

Fig. 10. SEM images showing the cross-sectional morphologies of Er_2O_3 coatings prepared with high rotational velocities: (a)/(a_1)/(a_2) macromorphology/high magnification, (b)/(b_1)/(b_2) macromorphology/high magnification.

Table 8
Estimated thicknesses and cross-sectional porosities of Er_2O_3 coatings prepared with a rotational velocity of 90 rpm and a powder flow rate of 20 g/min.

Samples	Carrier gas	Thickness (μm)	Cross-sectional porosity/SD (%)
(a)	O_2	124/11.1	10.3/0.19
(b)	N_2	145/8.0	23.3/0.96

Declaration of competing interest

The authors declared that they have no conflicts of interest to this work.

We declare that we do not have any commercial or associative interest that represents a conflict of interest in connection with the work.

Data availability

Data will be made available on request.

Acknowledgment

This research was supported by the National Natural Science Foundation of China (Grant #52071329); the Youth Innovation Promotion

Association of the Chinese Academy of Sciences, China (Grant #2020299); and the S&T Innovation 2025 Major Special Programme of Ningbo (Grant #2020Z095).

References

[1] Y. Dan, Y. Wang, A. Nakamura, H. Saitoh, H. Li, Effect of microstructure on the thermal conductivity of thermal barrier coating deposited by chelate-flame spraying, Ceram. Int. 48 (9) (2022) 12996–13005.
[2] M. Fukumoto, K. Yang, K. Tanaka, T. Usami, T. Yasui, M. Yamada, Effect of substrate temperature and ambient pressure on heat transfer at interface between molten droplet and substrate surface, J. Therm. Spray Technol. 20 (2011) 48–58.
[3] A. Khalid, M. Abbas, Y. Zhang, M. Hyland, P.R. Munroe, Microstructural study of Ni and Ni-20Cr particles plasma sprayed on stainless steel substrate at 300 °C, Appl. Surf. Sci. 592 (2022), 153320.
[4] C. Huang, A. List, J. Shen, B. Fu, S. Yin, T. Chen, B. Klusemann, F. Gärtner, T. Klassen, Tailoring powder strengths for enhanced quality of cold sprayed Al6061 deposits, Mater. Des. 215 (2022), 110494.
[5] Y. Zhang, S. Matthews, D. Wu, Y. Zou, Interactions between successive high-velocity impact droplets during plasma spraying, Surf. Coat. Technol. 431 (2022), 128006.
[6] A.S.M. Ang, C.C. Berndt, Investigating the anisotropic mechanical properties of plasma sprayed yttria-stabilized zirconia coatings, Surf. Coat. Technol. 259 (2014) 551–559.
[7] B.A. Kahl, Y.S. Yang, C.C. Berndt, A.S.M. Ang, Data-constrained modeling with multienergy X-ray computed microtomography to evaluate the porosity of plasma sprayed ceramic coatings, Surf. Coat. Technol. 436 (2022), 128267.
[8] A. McDonald, C. Moreau, S. Chandra, Thermal contact resistance between plasma sprayed particles and flat surfaces, Int. J. Heat Mass Transf. 50 (2007) 1737–1749.
[9] S. Yao, C. Li, J. Tian, G. Yang, C. Li, Conditions and mechanisms for the bonding of a molten ceramic droplet to a substrate after high-speed impact, Acta Mater. 119 (2016) 9–25.
[10] S. Brossard, P. Munroe, A. Tran, M. Hyland, Study of the effects of surface chemistry on splat formation for plasma sprayed NiCr onto stainless steel substrates, Surf. Coat. Technol. 204 (9–10) (2010) 1599–1607.
[11] M. Abbas, A. Khalid, G.M. Smith, P.R. Munroe, Investigation into the formation of ni splats plasma-sprayed on to mild steel and stainless steel substrates, Surf. Coat. Technol. 433 (2022), 128095.
[12] E. Bakan, D. Marcano, D. Zhou, Y. Sohn, G. Mauer, R. Vaßen, Yb2Si2O7 environmental barrier coatings deposited by various thermal spray techniques: a preliminary comparative study, J. Therm. Spray Technol. 26 (6) (2017) 1011–1024.
[13] X. Zhong, Y.R. Niu, H. Li, H.J. Zhou, S.M. Dong, X.B. Zheng, C.X. Ding, J.L. Sun, Thermal shock resistance of tri-layer Yb2SiO5/ Yb2Si2O7/Si coating for SiC and SiCmatrix composites, J. Am. Ceram. Soc. 101 (10) (2018) 4743–4752.
[14] J. Huang, R. Liu, Q. Hu, Y. Wang, X. Guo, X. Lu, M. Xu, Y. Tu, J. Yuan, L. Deng, J. Jiang, S. Dong, L. Liu, M. Chen, X. Cao, Effect of deposition temperature on phase composition, morphology and mechanical properties of plasma-sprayed Yb2Si2O7 coating, J. Eur. Ceram. Soc. 41 (2021) 7902–7909.
[15] M.P. Planche, H. Liao, B. Normand, C. Codde, Relationships between NiCrBSi particle characteristics and corresponding coating properties using different thermal spraying processes, Surf. Coat. Technol. 200 (2005) 2465–2473.
[16] K.N. Lee, Yb2Si2O7 environmental barrier coatings with reduced bond coat oxidation rates via chemical modifications for long life, J. Am. Ceram. Soc. 102 (3) (2019) 1507–1521.
[17] D.B. Proud, M.J. Evans, Q.N. Chan, P.R. Medwell, Dilute spray flames of ethanol and -heptane in the transition to mild combustion, Combust. Flame 238 (2022), 111918.
[18] R. Priya, S. Kainth, D. Kumar, P. Sharma, P.K. Diwan, O.P. Pandey, Investigating transformation kinetics of yttrium hydroxide to yttrium oxide, Mater. Chem. Phys. 287 (2022), 126243.
[19] P. Ctibor, J. Sedlacek, R. Musalek, T. Tesar, F. Lukac, Structure and electrical properties of yttrium oxide sprayed by plasma torches from powders and suspensions, Ceram. Int. 45 (6) (2022) 7464–7474.
[20] H. Akasaka, M. Ohto, Y. Hasebe, A. Nakamura, S. Ohshio, H. Saitoh, Yttria coating synthesized by reactive flame spray process using Y-EDTA complex, Surf. Coat. Technol. 205 (2011) 3877–3880.
[21] K. Komatsu, T. Sekiya, A. Toyama, Y. Hasebe, A. Nakamura, M. Noguchi, Y. Li, S. Ohshio, H. Akasaka, H. Muramatsu, H. Saitoh, Deposition of metal oxide films from metal–EDTA complexes by flame spray technique, J. Therm. SprayTechnol. 23 (2014) 833–838.
[22] Y. Dan, T. Costa, A. Nakamura, K. Komatsu, H. Saitoh, Effect of in-flight particle behavior on the morphology of flame sprayed Er2O3 splats, Ceram. Int. 47 (2021) 11862–11869.
[23] K. Komatsu, T. Shirai, A. Toyama, T. Iseki, Y. Dan, T. Costa, Y. Li, S. Ohshio, H. Muramatsu, A. Nakamura, H. Saitoh, Densification of metal oxide films synthesized from metal complexes by flame spraying, Surf. Coat. Technol. 325 (2017) 89–97.
[24] Y. Dan, X. Zhou, A. Nakamura, K. Komatsu, H. Saitoh, Splat morphology and microstructure of chelate flame sprayed Er2O3 films, J. Ceram. Soc. Jpn. 128 (2020) 945–953.
[25] Y. Dan, T. Costa, Z. Guo, A. Nakamura1, K. Komatsu, H. Saitoh, Thermal barrier coatings formed by flame spray with metal-EDTA, Jpn. J. Appl. Phys. 59 (2020), 75507.
[26] K. Komatsu, A. Toyama, T. Sekiya, T. Shirai, A. Nakamura, I. Toda, S. Ohshio, H. Muramatsu, H. Saitoh, Flame-sprayed Y2O3 films with metal-EDTA complex using various cooling agents, J. Therm. SprayTechnol. 26 (2017) 195–202.
[27] D. Chen, F. Luo, X. Lou, Y. Qing, W. Zhou, D. Zhu, Comparison of thermal insulation capability between conventional and nanostructured plasma sprayed YSZ coating on Ni3Al substrates, Ceram. Int. 43 (2017) 4324–4329.
[28] R. Ghasemi, H. Vakilifard, Plasma-sprayed nanostructured YSZ thermal barrier coatings: thermal insulation capability and adhesion strength, Ceram. Int. 43 (2017) 8556–8563.
[29] K. Komatsu, T. Costa, Y. Ikeda, K. Abe, Y. Dan, T. Kimura, A. Nakamura, T. Shirai, H. Saitoh, Synthesis of Y2O3 films on an aluminum alloy substrate using flame-spray apparatus with a H2–O2 flame, Int. J. Appl. Ceram. Technol. 16 (1) (2019) 254–263.
[30] Y.X. Dan, K. Komatsu, K. Keita, T. Costa, Y. Ikeda, A. Nakamura, S. Ohshio, H. Saitoh, Heat-shock properties in yttrium-oxide films synthesized from metal-ethylenediamine tetraacetic acid complex through flame-spray apparatus, Appl. Phys. A Mater. Sci. Process. 123 (2017) 194.
[31] M.A. Mulero, J. Zapata, R. Vilar, V. Martínez, R. Gadow, Automated image inspection system to quantify thermal spray splat morphology, Surf. Coat. Technol. 278 (2015) 1–11.
[32] F. Fanicchia, D.A. Axintea, J. Kellb, R. McIntyreb, G. Brewsterb, A.D. Nortonb, Combustion flame spray of CoNiCrAlY & YSZ coatings, Surf. Coat. Technol. 315 (2017) 546–557.
[33] F.D. Savkar, P.A. Siemers, Some recent developments in rapid solidification plasma deposition technology, in: M. Boulos (Ed.), ISPC-9 Workshop on Industrial Plasma Applications, 1989, pp. 80–89. Pugnochiuso, Italy, Sep 9–10.
[34] M. Mutter, G. Mauer, R. Mücke, O. Guillon, R. Vaßena, Correlation of splat morphologies with porosity and residual stress in plasma-sprayed YSZ coatings, Surf. Coat. Technol. 318 (2017) 157–169.
[35] C.W. Kang, H.W. Ng, Splat morphology and spreading behavior due to oblique impact of droplets onto substrates in plasma spray coating process, Surf. Coat. Technol. 200 (2006) 5462–5477.
[36] S. Chen, G. Ma, H. Wang, P. He, Z. Liu, Solidification mechanism and quantitative characterization of fe-based amorphous splat formed by plasma sprayed droplets with different in-flight status, J. Alloy. Compd. 768 (2018) 789–799.
[37] B. Huang J. Wang Z. Tang W. Li W. Zhu R. Gu Fluoride-mediated corrosion mechanism of atmospheric-plasma-sprayed yttrium–aluminum garnet ceramic coatings, J. Eur. Ceram. Soc., doi.org/10.1016/j.jeurceramsoc.2022.06.012.
[38] R. Dhiman, S. Chandra, Freezing-induced splashing during impact of molten metal droplets with high weber numbers, Int. J. Heat Mass Transf. 48 (25) (2005) 5625–5638.